



1 **Estimation of rainfall erosivity based on WRF-derived raindrop size distributions**

2 Qiang Dai^{1,2}, Jingxuan Zhu¹, Shuliang Zhang¹, Shaonan Zhu³, Dawei Han² and Guonian Lv¹

3 ¹Key Laboratory of VGE of Ministry of Education, Nanjing Normal University, Nanjing, China.

4 ²Department of Civil Engineering, University of Bristol, Bristol, UK.

5 ³College of Geographical and Biological Information, Nanjing University of Posts and
6 Telecommunications, Nanjing, China

7 Corresponding author: Qiang Dai (qd_gis@163.com)

8 **Key Points:**

- 9 • WRF-derived rainfall kinetic energy offers a novel way to estimate large-scale soil
10 erosion.
- 11 • Annual rainfall and erosivity are not always positively correlated.
- 12 • Highest rainfall erosivity of UK occurs in the west coast area during 2013-2017.
- 13



14 **Abstract**

15 Soil erosion can cause various ecological problems, such as land degradation, soil fertility loss,
16 and river siltation. Rainfall is the primary water-driving force for soil erosion and its potential
17 effect on soil erosion is reflected by rainfall erosivity that relates to the raindrop kinetic energy
18 (KE). As it is difficult to observe large-scale dynamic characteristics of raindrops, all the current
19 rainfall erosivity models use the function based on rainfall amount to represent the raindrops KE.
20 With the development of global atmospheric re-analysis data, numerical weather prediction
21 (NWP) techniques become a promising way to estimate rainfall KE directly at regional and
22 global scales with high spatial and temporal resolutions. This study proposed a novel method for
23 large-scale and long-term rainfall erosivity investigations based on the Weather Research and
24 Forecasting (WRF) model, avoiding errors caused by inappropriate rainfall–energy relationships
25 and large-scale interpolation. We adopted three microphysical parameterizations schemes
26 (Morrison, WDM6, and Thompson aerosol-aware [TAA]) to obtain raindrop size distributions,
27 rainfall KE and rainfall erosivity, with validation by two disdrometers and 304 rain gauges
28 around the United Kingdom. Among the three WRF schemes, TAA had the best performance
29 compared with the disdrometers at a monthly scale. The results revealed that high rainfall
30 erosivity occurred in the west coast area at the whole country scale during 2013-2017. The
31 proposed methodology makes a significant contribution to improving large-scale soil erosion
32 estimation and for better understanding microphysical rainfall–soil interactions to support the
33 rational formulation of soil and water conservation planning.

34

35 **1 Introduction**

36 Soil erosion has a pivotal role in shaping the Earth’s physical landscape; however, it can
37 threaten both ecosystems and human societies (Alewell et al., 2015). Accurate quantification of
38 soil loss impact at large spatial scales is therefore important for developing land-use planning
39 and sustainable conservation practices (Bilotta et al., 2012). The soil erosion rate is driven by a
40 combination of factors, which include rainfall, topography, soil characteristics, land cover, and
41 land management applications (Wischmeier and Smith, 1958; Panagos et al., 2015b). Among
42 these, rainfall is a driving force that accounts for a large proportion of soil loss throughout most
43 of world (Panagos et al., 2015b). The erosive force of rainfall with consequent runoff is



44 represented as erosivity of rainfall, which is a crucial factor for estimating soil loss in large-scale
45 soil erosion models; for instance, the Universal Soil Loss Equation (USLE (Wischmeier and
46 Smith, 1978) or RUSLE (Renard et al., 1997)), Limburg Soil Erosion Model (LISEM) (De Roo
47 et al., 1996), and USLE-M (Kinnell and Risse, 1998).

48 Rainfall erosivity estimation involves the microphysical properties of rainfall and
49 rainfall–soil interactions on different time steps (Petan et al., 2010). Impact of rainfall, the main
50 mechanism driving the splashing of soil particles from the soil mass, which leads to soil erosion
51 through soil disintegration and mobilization, relies on the kinetic energy (KE) of raindrop
52 motions (Wischmeier and Smith, 1958; Wang et al., 2014). Robust measurement of raindrop size
53 and terminal velocity is vital for estimating and predicting rainfall erosivity. Many measurements
54 can be used to obtain these two parameters, including the stain paper or flour pellet methods
55 (Marshall and Palmer 1948; Wischmeier and Smith, 1958), high speed cameras (Jones, 1959;
56 Kinnell, 1981; McIsaac, 1990), and disdrometers (Petan et al., 2010; Angulo-Martinez et al.,
57 2012). Accurate measurements of raindrop size can be provided in all their methods, and
58 terminal velocity of raindrops can be further measured by video cameras and disdrometers.
59 Velocity can also be estimated as the function of raindrop diameter from the empirical
60 relationship (Beard, 1976; Atlas and Ulbrich, 1977; Uplinger, 1981; Van Dijk et al., 2002).
61 When using ground observations, rainfall KE can be estimated at a given site.

62 However, direct measurement of rainfall KE in a large area is difficult because it requires
63 considerable effort, as well as a dense network of expensive instruments that provide accurate
64 outputs (Fornis et al., 2005; Mikoš et al., 2006; Meshesha et al., 2016; Dai et al., 2017). Previous
65 studies have therefore mainly employed more readily accessible records like rainfall intensity,
66 and attempted to estimate rainfall KE from the empirical relationship of unit KE (ke) with
67 intensity ($ke-I$). Since Marshall and Palmer (1948) first observed a two-parameter exponential
68 relationship between drop size and intensity, several forms of $ke-I$ mathematical expressions for
69 specific locations and climatic conditions have been proposed, including power-law (Park et al.,
70 1982; Meshesha et al., 2016), linear (Sempere-Torres et al., 1998; Nyssen et al., 2005),
71 polynomial (Carter et al., 1974), logarithmic (Wischmeier and Smith, 1978; Davison et al., 2005;
72 Meshesha et al., 2014), and exponential (Kinnell, 1981; Brown and Foster, 1987) relationships.
73 Among these, the exponential function has been preferentially used currently (Van Dijk et al.,
74 2002; Fornis et al., 2005; Petan et al., 2010; Sanchez-Moreno et al., 2012; Lim et al., 2015).



75 Accurate raindrop size distribution (DSD) measured by disdrometers is widely used to derive ke –
76 I relationships (Angulo-Mart ínez et al., 2016; Meshesha et al., 2016). However, such empirically
77 derived formulas indicate that rainfall ke will increase infinitely with increasing intensity,
78 whereas studies (Rosewell, 1986; Angulo-Mart ínez et al., 2016; Meshesha et al., 2019) have
79 found that rainfall ke reaches an top value when intensity is around 70 mm h^{-1} (Hudson, 1963;
80 Wischmeier and Smith, 1978). More importantly, such a ke – I relationship only represents local
81 climate and precipitation microphysics, and is valid for such regions. There is great uncertainty
82 associated with rainfall erosivity estimation using this ke – I relationship in a large domain
83 (Angulo-Mart ínez and Barros, 2015), especially due to the poor spatial and temporal
84 predictability of the ke – I relationship. This has motivated researchers to directly calculate KE
85 based on large-scale DSD measurements.

86 Ground- and space-based radar can be used to obtain DSD parameters (Atlas et al., 1973;
87 Doelling et al., 1998). For example, the space-borne Dual-frequency Precipitation Radar (DPR)
88 radar containing Ku- and Ka-bands in the Global Precipitation Measurement (GPM) satellite
89 allows researchers to estimate the global three-dimensional spatial distribution of hydrometeors.
90 Unfortunately, ground dual-polarization radars are available in limited areas (Prigent, 2010) with
91 large uncertainties (Dai et al., 2019), and the GPM DPR instrument, which measures DSD with
92 daily or longer temporal resolutions, fail to capture a full storm and meet the requirement for
93 rainfall kinetic estimation. Mesoscale numerical weather prediction models, for instance, the
94 WRF model, can simulate microphysical cloud processes and predict the evolution of particle
95 size distribution through computationally feasible parametrization schemes (Dai et al., 2014;
96 Brown et al., 2016). DSD on the ground can be derived from the WRF model through
97 consideration of various physical processes, types of hydrometeor, and free degrees of size
98 distributions in hydrometeor. As such, a number of recent researches have investigated the
99 retrieval and uncertainty of DSD parameters by WRF (Gilmore et al., 2004; Čurić et al., 2009;
100 Brown et al., 2016; Yang et al., 2019).

101 The WRF model runs with initial and boundary conditions using global reanalysis
102 datasets, such as those of the European Centre for Medium-range Weather Forecasts (ECMWF)
103 and National Centers for Environmental Prediction (NCEP). In other words, WRF-derived DSD
104 can be obtained for any given area with fine spatial and temporal resolutions rather than
105 traditional course linear interpolations. We therefore attempted to estimate rainfall erosivity for



106 the whole United Kingdom (UK) domain using WRF-derived DSD. For comparison, we
107 calculated interpolated traditional disdrometer-derived rainfall erosivity. To our knowledge, this
108 work is the first attempt to take advantage of a numerical weather prediction model for
109 estimating rainfall erosivity anywhere around the world. The current study contributes to the
110 development of large-scale soil erosion estimation and provides a better comprehension of
111 microphysical rainfall–soil interactions.

112 **2 Methodology**

113 2.1 Disdrometer-based rainfall KE estimation

114 KE dominates the ability of raindrop to separate soil particles. The KE (e , unit: J) of a
115 raindrop with mass m (g) and terminal velocity v (m s^{-1}) is defined by:

$$e = \frac{1}{2} mv^2 \quad (1)$$

116 Assuming a spherical volume for every raindrop shape, the mass of a drop can be
117 calculated from the cube of the diameter D (mm). Because instruments (e.g., disdrometers)
118 generally sample drop size, the mean radius and falling velocity of the corresponding sampling
119 drop-size class is used to represent D and v , expressed as D_i and v_i , respectively. In such cases,
120 the e_i with any drop of a given class is given as:

$$e_i = \frac{1}{12} 10^{-6} \pi \rho v_i^2 D_i^3 \quad (2)$$

121 where ρ is the water density (g cm^{-3}). The sum of the KE of each individual raindrop within a
122 given rain depth that hits a given area defines the total KE. The unit rainfall KE ke_t in the t^{th}
123 minute ($\text{MJ ha}^{-1} \text{mm}^{-1}$) can be calculated as the sum of each drop KE in each size set, as follows:

$$ke_t = \frac{e_{sum}}{AP_t} = \frac{1}{AP_t} \sum_{i=1}^{n_i} N_i e_i \quad (3)$$

124 where A represents the sample area of the sensor, P_t is rainfall depth at time t , and N_i is the drops
125 number in class i . The instrument sums up the number of raindrops in each sampling class and
126 produces the raindrop spectra for a time step. Here, we use the term ke to represent the
127 disdrometer-based KE estimated by DSD measured directly every minute. The terminal velocity



128 of a raindrop can be estimated from its power law empirical relationship with raindrop diameter
129 (Atlas and Ulbrich, 1977), with this considered more suitable for Chilbolton in the UK (Islam et
130 al., 2012):

$$v_{Atl} = 3.78D_i^{0.67} \quad (4)$$

131 Thus, unit rainfall KE estimates per minute are obtained by replacing v_i in Eq. (2) with v_{Atl} .

132 The other form of rainfall KE is expressed at an event scale and represents the sum of the
133 storm energy covering all time steps covering an event. The individual event energy (MJ ha^{-1}) is
134 calculated as follows:

$$E = \sum_{t=1}^{nt} ke_t P_t \quad (5)$$

135 where P_t is the rainfall amount (mm) in the t^{th} minute and nt is the time steps number. Historical
136 rainfall data are divided into wet and dry periods. A string of erosive rainfall storms are first
137 extracted through the predefined rules. A continuous 6-h dry period interval was used to divide
138 rainfall events (Hanel et al., 2016), following the “minimum dry-period duration” definition of a
139 rainfall event (Bonta, 2004). Moreover, a rainfall amount of 12.7 mm was set as the threshold to
140 filter effective rainfall events (Renard et al., 1997).

141 Rainfall KE is obtained for a given site based on size and velocity of raindrops. When
142 disdrometer data are absence, energy can be estimated from empirical relationships using rainfall
143 intensity I (mm). Five commonly used functions (including exponential, logarithmic, power law,
144 and inverse proportion) have been mentioned in Section 1. Taking the exponential form as an
145 example, the rainfall KE at any location can be estimated as:

$$E_{\max} = e_{\max}(1 - ae^{-bI}) \quad (6)$$

146 where e_{\max} is the mean maximal value of energy measured under high rainfall intensity, and a
147 and b are coefficients modeling the equation curve. Here, minimum KE can be determined by
148 parameters a and e_{\max} together, while the overall shape of the curve is modeled by parameter b .



149 2.2 WRF-based rainfall KE estimation

150 Differing from disdrometer measurements, the complete DSD cannot be obtained from
151 the WRF model. Instead, the DSD of the microphysical parameterization (MP) scheme is
152 handled with a constrained-gamma distribution model, which is defined as:

$$N(D) = N_0 D^\mu e^{-\lambda D} \quad (7)$$

153 where N_0 , μ , and λ are the intercept, shape, and slope parameters of the DSD. In terms of double-
154 moment bulk schemes, N_0 and λ can be abstracted from the number concentration N and
155 predicted mixing ratio q , as shown below:

$$N_0 = \frac{N \lambda^{\mu+1}}{\Gamma(\mu + 1)} \quad (8)$$

$$\lambda = \left[\frac{c M \Gamma(\mu + d + 1)}{q \Gamma(\mu + 1)} \right]^{\frac{1}{d}} \quad (9)$$

156 c and d are the assumed power-law coefficients between diameter and mass ($m = cD^d$), and Γ
157 represents the function in gamma form (Morrison et al., 2009). The value of the shape parameter
158 μ ($\mu = 0$) in double-moment schemes is fixed, except for the WRF double-moment 6-class
159 (WDM6) schemes, following gamma distribution which defined $\mu = 1$ (Jung et al., 2010;
160 Johnson et al., 2016).

161 Because DSD retrieval is sensitive to MPs (Cintineo et al., 2014; Morrison et al., 2015),
162 the WRF model this study adopted completely or partially three types of double-moment cloud
163 MP schemes. The Morrison double-moment scheme involves the number concentrations and
164 mixing ratios of multiple hydrometeors (Morrison et al., 2009). Moreover, the WDM6 scheme
165 further considers a prognostic factor to estimate and predict the cloud condensation nuclei (CCN)
166 number concentration (Hong et al., 2010; Lim and Hong, 2010). Finally, the Thompson aerosol-
167 aware (TAA) scheme can predict both ice nuclei (IN) and CNN number concentrations
168 (Thompson and Eidhammer, 2014).

169 The DSD parameters were thus obtained under the three WRF MPs. For theoretical DSD,
170 ke estimates per minute were obtained by integration of the full raindrop size spectrum using:



$$ke'_t = \frac{1}{AR_t} \int_0^\infty N(D) \frac{1}{12} 10^{-6} \pi \rho v_i^2 D_i^3 dD \quad (10)$$

171 For the WRF-derived DSD covering the whole study area, there was no need to construct
172 a ke - I relationship to interpolate KE in ungauged areas. The WRF-based rainfall KE under storm
173 event scale is thus given as:

$$E_{\#} = \sum_{t=1}^{nt} ke'_t P_t \quad (11)$$

174 2.3 Rainfall erosivity estimation

175 Most storm events have relatively low intensities and KEs with occasional peaks, based
176 on the disdrometer DSD data used to evaluate the rainfall ke - I function. Proper estimation of
177 rainfall erosivity potential should consider total KE over a long period. The rainfall erosivity
178 factor (or R-factor) is calculated by a multi-annual average of the total storm erosivity index
179 (Wischmeier and Smith, 1958; Van Dijk et al., 2002), while annual rainfall erosivity R can be
180 obtained using:

$$R = \sum_{m=1}^M (EI_{30})_m \quad (12)$$

181 where M is the total number of erosive events within a year. $(EI_{30})_m$ are total rainfall kinetic
182 energy and maximum 30-min rainfall intensity recorded within 30 consecutive minutes (unit:
183 mm h^{-1}), respectively, for the m^{th} event.

184 Wischmeier and Smith (1958) first proposed the use of EI_{30} , as the rainfall erosivity for
185 each event, based on research data from many sources. I_{30} was calculated to have higher
186 relevance to soil erosion than maximum 5-min, 15-min, or 60-min rainfall intensities
187 (Wischmeier and Smith, 1958). The calculation of EI_{30} initially uses recording-rain gauge data to
188 divide continuous rainfall into time periods with equal rainfall intensity. Because rainfall
189 measurements with high temporal resolutions are required but difficult to obtain from general
190 rainfall measurements, short time equal-interval rainfall data with higher accuracy over multiple
191 years are preferred for estimating EI_{30} . For example, Xie et al. (2016) used 1-min rainfall data
192 instead of recording-rain gauge records. For coarse-resolution, equally spaced data, researchers



193 have proposed a conversion factor to reduce bias error (Weiss, 1964; Williams and Sheridan,
194 1991).

195 The rainfall erosivity can be derived from rainfall KE. It plays a main dynamic role in
196 USLE/RUSLE, representing the potential for soil erosion caused by rainfall. To distinguish the
197 disdrometer- and WRF-derived rainfall erosivity in this study, we use the terms R_D and R_W ,
198 respectively.

199 2.4 Evaluation methods

200 Because there is no direct way to measure rainfall erosivity across a large area, it is
201 difficult to validate outcomes using observations. However, R_D is considered to be relatively
202 accurate due to its specific measurement of raindrops. We therefore assumed that R_W values were
203 accurate if it closely matched R_D of a given location. A long-term comparison of R_W and R_D at
204 disdrometer stations was thus conducted to evaluate the validity of R_W .

205 Three indicators were introduced for the evaluation: Pearson's correlation coefficient,
206 mean absolute error (MAE), and coefficient of determination (R^2) (Borrelli et al., 2017). Pearson
207 correlation coefficient is an index used to evaluate the linear correlation between two variables,
208 and is defined as follows:

$$Pearson = \frac{n \sum R_{D_i} \sum R_{W_i} - \sum R_{D_i} \sum R_{W_i}}{\sqrt{n \sum R_{D_i}^2 - (\sum R_{D_i})^2} \sqrt{n \sum R_{W_i}^2 - (\sum R_{W_i})^2}} \quad (13)$$

209 where n is the number of variable samples. Because this correlation cannot reveal the absolute
210 bias of rainfall erosivity values, the MAE was also used; this is defined as:

$$MAE = \frac{\sum |R_{W_i} - R_{D_i}|}{n} \quad (14)$$

211 R^2 is an indicator to assess the fit of the trend line, expressed as the ratio of the variance
212 in the dependent variable predicted from the independent variable. It measures the extent to
213 which the model replicates observations based on the proportion of the results interpreted by the
214 model to the total change, written as:



$$R^2 = 1 - \frac{SS_{res}}{SS_{tot}} \quad (15)$$

215 where SS_{res} is the sum of squares of residuals between two variables and SS_{tot} is the total sum of
216 squares.

217 **3 Study area and data sources**

218 The whole of the UK was set as the experimental area for investigating rainfall erosivity
219 estimation. The UK consists of mostly lowland terrain, with a maximum elevation of 1345 m.
220 Water and wind are most significant forces of soil erosion in the UK, and together cause
221 approximately 2.2 million tons of topsoil to be eroded annually, seriously affecting soil
222 productivity, water quality, and aquatic ecosystems through siltation of watercourses (EA, 2004).
223 According to the Environmental Agency, the total cost of soil erosion in the UK is approximately
224 \$88 million each year, including an agricultural production loss of \$17.6 million (O'Neill, 2007).
225 More importantly, the changing climate may exacerbate the degree of erosion. For example,
226 hotter, drier climates make soils more susceptible to wind erosion, and intense storms increase
227 rainfall erosivity (Defra, 2009). Studies of water erosion in England and Wales (Morgan, 1985;
228 Evans, 1990) have found that loose soils (especially sand), such as the soils found in Shropshire
229 and Herefordshire in Wales, are more susceptible to water erosion. In a study of rainfall erosion
230 in Europe, Panagos et al. (2015a) found that the humid Atlantic climate results in highly variable
231 rainfall erosivity, such as higher R-factor values in western England and lower values in the
232 eastern UK.

233 The gauge datasets used are from the land surface and marine surface measurements
234 datasets (data availability: 1853–present) provide by the UK Met Office. A network of rain
235 gauges covering 304 stations across the whole UK observes continuous rainfall data in hours
236 (Figure 1). The base data of most stations comprises the times of each tip (0.2 mm per tip),
237 converted into 1-h rain accumulations. The rainfall observations are not always valid for each
238 hour at each station. The hourly grid-based rainfall maps are then calculated based on ordinary
239 kriging interpolation of rain gauge network data to obtain the spatial distribution of rainfall for
240 each time step, as inputs for rainfall erosivity estimation. This wide-range-use geostatistical
241 approach can account for both the distance and pairwise spatial relationship between points



242 through variograms. The precipitation interpolation method uses sample gauge points taken at
243 different locations and creates a continuous surface to achieve an accurate spatial variation
244 estimation of rainfall patterns.

245 We used data from two disdrometers in southern England. The first was Chilbolton
246 station (51°08'N, 1°26'W), with an impact-type Joss–Waldvogel disdrometer (JWD) mainly
247 used to compute rainfall erosivity. It can measure drop sizes from 0.3 to 5.0 mm in 127 bins. The
248 sampling period and collector area were 10 s and 50 cm², respectively. Data were available for
249 April 2003 to July 2018. The second was the University of Bristol station (51°27'N, 2°36'W),
250 with an OTT Parsivel² disdrometer (OPD). Data were available for November 2015 to December
251 2018. This disdrometer subdivides particles into appropriate classes and has a nominal cross-
252 sectional area of 54 cm². The 10-s period measurement data from the two disdrometers were
253 averaged into a 1-min period to filter out time variations (Montopoli et al., 2008; Islam et al.,
254 2012; Song et al., 2017).

255 Meteorological data comes from the ERA-Interim dataset, a global atmosphere re-
256 analysis product, generated by the ECMWF. For the scientific community, ERA-Interim is
257 considered to be one of the most important atmospheric datasets, with its data rich period
258 available since 1979 and updated in current time (Dee et al., 2011). The Integrated Forecasting
259 System released in 2006 contains a 12-h analysis window derived 4-D variational analysis,
260 driving the data assimilation system to generate ERA-Interim. The dataset covers 60 vertical
261 classes of approximately 80 km from the ground to 0.1 hPa. The Gridded Binary format is used
262 to store data for three months in a separate file. A data processing scheme was established to
263 collect and retrieve ERA-Interim data of each rainfall event.

264 The rain gauge and Chilbolton disdrometer datasets can be obtained from British
265 Atmospheric Data Centre in National Centre for Atmospheric Science research center (MO,
266 2012). ERA-Interim data can be obtained from the ECMWF Public Dataset website
267 (<https://apps.ecmwf.int/>). Considering the availability of the above datasets and model
268 requirements, we mainly used data covering the period 2004–2017.



269 4 Results

270 4.1 Empirically derived rainfall erosivity estimation

271 To evaluate the R_W , the raindrop spectrum collected by the Chilbolton station disdrometer
272 is used to estimate rainfall KE first. The key in estimating rainfall KE by disdrometer lies on
273 building an empirical relationship between rainfall amount and KE. We used DSD measurements
274 from 2004 to 2013 to establish five empirical relationships between unit rainfall kinetic energy
275 (ke) and intensity (I) (Table 1), and used 2014–2017 data for the cross validation. It can be seen
276 from Table 1 that the inverse proportional relationship (Equation III in Table 1) had the worst
277 performance, in that both the calibration and validation R^2 values were < 0.3 . The values of the
278 other equations were > 0.48 , among which the exponential formula (Equation I in Table 1) had
279 the highest calibration R^2 (0.50) and validation R^2 (0.45), respectively. In addition, the power
280 law formula (Equation V in Table 1) showed a similar performance to the exponential formula at
281 rainfall intensities $< 5 \text{ mm h}^{-1}$. However, the power law formula also had a continuous
282 increasing trend, which may not be suitable for high-intensities. Figure 2 shows the fitted
283 relationship of $ke-I$ based on exponential regression. The exponent-based relationship is widely
284 used in the literature and in forecast models such as RUSLE (Renard et al., 1997). We therefore
285 adopted it here as the empirical formula to estimate rainfall erosivity in the UK.

286 Based on rainfall KE, the point R_D can be obtained at a disdrometer location. In current
287 study, we established a method to estimate the R-factor using 60-min rainfall data. EI_{30} obtained
288 from 1-min DSD data was considered as the standard R-factor at Chilbolton Station. Hourly rain
289 gauge data at the same location were used to calculate $(EI_{30})_{60}$, which refers to EI_{30} calculated
290 from 60-min data. The regression relationship between EI_{30} and $(EI_{30})_{60}$ was then established.
291 The $(EI_{30})_{60}$ of each month, obtained from the 60-min rainfall data of the Chilbolton Station rain
292 gauge in 2004–2013, was calculated. The regression relationship between the monthly sum of
293 $(EI_{30})_{60}$ and the standard monthly EI_{30} from DSD was calculated to obtain a coefficient of 1.836.
294 Rainfall erosivity can subsequently be calculated by multiplying $(EI_{30})_{60}$ by the coefficient.

295 Beyond assuming that the disdrometer-derived $ke-I$ relationship can be applied to a
296 whole study area; point rainfall measurements must be interpolated to obtain areal rainfall values
297 in traditional rainfall erosivity estimation. We obtained 60-min rainfall data from 304 rain gauges
298 around the UK from 2004 to 2017. Note that not all rain gauges were available for the whole



299 period (available gauges each year are indicated in Figure 3). We used the ordinary kriging
300 interpolation method to obtain the spatial distribution of rainfall for each time step. This wide-
301 range-use geostatistical approach can account for both the distance and pairwise spatial
302 relationship between points through variograms. Figure 3 shows the results of annual rainfall
303 (*Rain*), annual rainfall kinetic energy (*E*), and annual rainfall erosivity (*R*) for different years.
304 The distribution trends of *Rain*, *E*, and *R* were similar, and were positively correlated except for
305 certain locations or periods. For instance, in 2013, *Rain* in the northwestern UK decreased from
306 west to east, while *E* and *R*-factor decreased from south to north; furthermore, areas with large *E*
307 and *R* values in southeastern UK could not be directly observed from the rain map.

308 The key concern in traditional rainfall erosivity estimation is the spatial predictability of
309 the *ke-I* relationship. To verify the regional reliability of this relationship, we used data from a
310 newer disdrometer located at the University of Bristol, approximately 87 km from Chilbolton
311 Station. The validation data at Bristol Station discontinuously covered the period 2016–2019.
312 Figure 4 shows the exponential relationship of *ke-I* at Bristol station, which differed
313 substantially from that based on data from Chilbolton station. A comparison of the modeled and
314 observed event rainfall erosivity is shown in Figure 5. The modeled erosivity of rainfall event
315 was not consistent with the observed event rainfall erosivity. The linear regression coefficient
316 between these values was > 1.2 , which was the result of the low *ke* for Bristol Station, and R^2
317 was < 0.85 , indicating large uncertainty associated with disdrometer-based rainfall erosivity
318 estimation.

319 In summary, the point rainfall erosivity estimated by disdrometer is considered to be
320 accurate compared to other methods. However, a large-scaled rainfall erosivity through a simple
321 interpolation of rainfall KE is subjected to a large uncertainty. In the following analysis, the
322 point R_D is used to appraise the performance of proposed WRF-based estimated method, and the
323 R_D in the whole UK is only be used for a general comparison of spatial and temporal distribution
324 of rainfall erosivity.

325 4.2 Rainfall and DSD estimation by WRF

326 We used the WRF model ver. 3.8, which has an Advanced Research WRF dynamical
327 core, to downscale the ERA-Interim reanalysis data. The double-nested domain configuration
328 used in the WRF model was centered at 55 °19'N, 2 °21'W and applied at a downscaling ratio of



329 1:5, a finest grid of 5 km, and a temporal resolution of 1 h. Table 2 lists the detailed parameters
330 used in this domain configuration. With the top pressure level set at 50 hPa in each, both
331 domains include 28 vertical levels. To obtain favorable initial weather conditions, the model ran
332 continuously to obtain five years of WRF simulation results.

333 Simulations were performed using three different bulk double moment MPs: the
334 Morrison (Morrison et al., 2009), WDM6 (Hong et al., 2010; Lim and Hong, 2010) and TAA
335 (Thompson and Eidhammer, 2014) schemes. All three can predict the number concentration and
336 hydrometeors mixing ratio each time step. The WDM6 scheme also predicts the number
337 concentration of CCN (Hong et al., 2010; Lim and Hong, 2010), while the TAA scheme are able
338 to predict both IN and CCN number concentrations (Thompson and Eidhammer, 2014).
339 Additionally, other physical parameterizations include the Dudhia shortwave radiation scheme
340 (Dudhia, 1989), Mellor–Yamada–Janjic planetary boundary layer scheme (Janjić, 1994), RRTM
341 longwave radiation scheme (Mlawer et al., 1997), the Noah land-surface model (Ek et al., 2003),
342 and the Kain–Fritsch cumulus scheme (Kain, 2004),.

343 The median volume diameter parameter (D_0) and generalized intercept parameter (N_w)
344 are generally used in DSD model of WRF (Islam et al., 2012).

$$N_w = \frac{N_0 D_m^\mu}{f(\mu)} \quad (16)$$

$$f(\mu) = \frac{6(4 + \mu)^{\mu+4}}{4^4 \Gamma(\mu + 4)} \quad (17)$$

345 where D_m is the mass-weighted mean diameter. The $f(\mu)$ is a function of the shape parameter μ .
346 The parameter μ is assumed as zero or one (based on microphysical scheme configuration) in
347 WRF. Figure 6 displays the spatial distribution of D_0 and generalized intercept parameter N_w for
348 a given day with rainfall countrywide (January 10, 2013). D_0 and N_w had similar patterns, and
349 were mainly distributed across the southwestern and northeastern UK. The white strip in the
350 middle of Figure 6 represents an area that received no rain. However, the three MPs yielded large
351 differences; D_0 of MP-TAA was the highest among three MPs, whereas N_w of MP-WDM6 was
352 much larger than others. In addition, D_0 and N_w did not consistently show a positive correlation.



353 The different MP estimation results underscore the complexity of the rainfall process, which is
354 the reason we estimated rainfall KE using WRF schemes instead of traditional formulas.

355 4.3 Comparison of WRF- and disdrometer-derived rainfall erosivity at Chilbolton station

356 With the WRF-based rainfall intensity and DSD estimations, rainfall erosivity was
357 derived using Equations (10)–(12). Hereafter, this is referred to as R_W , which is further
358 distinguished based on the three MP schemes used: $R_{W-Morrison}$, R_{W-WDM6} , and R_{W-TAA} . Figure 7
359 compares disdrometer- and WRF-derived monthly rainfall erosivity estimations at Chilbolton
360 Station for the period 2014–2017. The general patterns of the four rainfall erosivity values were
361 similar. $R_{W-Morrison}$ tended to be larger than R_D in some months, whereas R_{W-TAA} matched the R_D
362 value relatively well for smaller values. Because WRF data were taken from a 2×2 -km grid
363 around Chilbolton Station, there was spatial error in addition to the systematic error of estimating
364 rainfall erosivity.

365 Table 3 shows the correlation indicator results between R_D and the three type R_W at
366 Chilbolton station. The Pearson correlation coefficients generally exceeded 0.7, supporting the
367 potential utility of WRF-based estimation. In terms of MAE, R_{W-TAA} had the best performance
368 (6.51), whereas $R_{W-Morrison}$ and R_{W-WDM6} showed slightly worse performance (approximately 8).
369 Among the three schemes, R_{W-TAA} had the best fit with R_D . The indicators and comparison results
370 suggest that the deviations in results need to be considered; a method of bias elimination is
371 therefore described in Section 4.4.

372 4.4 R_W estimation for the whole UK

373 The R_W at Chilbolton station showed obvious systematic deviations compared with the
374 disdrometer-derived results (see Section 4.2 and 4.3). A simple bias correction was therefore
375 applied to adjust the individual storm KE estimations of R_W . The biases from dividing average
376 $R_{W-Morrison}$, R_{W-WDM6} , and R_{W-TAA} by average R_D during 2014–2017 were 0.55, 0.20, and 0.36,
377 respectively.

378 The rainfall erosivity distribution for the whole UK was then obtained. Figure 8 shows
379 the distribution of R_W at the annual scale covering the period 2013–2017. The pattern of the
380 rainfall erosivity maps showed a general regional-dominant characteristic. For example, it
381 always decreased from west to east, predominantly shaped by orography. Affected by the



382 prevailing westerly winds, there was abundant rainfall in the western and northern mountains, as
383 indicated by high rainfall KE values in these regions. In addition, among the study years, 2014
384 and 2015 showed higher national rainfall erosivity, with a large range in the west coast area.

385 Figure 9 shows the average R distribution for 2013–2017 estimated by rain gauges and
386 WRF MPs. WRF grids could cover all regions in the UK evenly, offering more detailed erosivity
387 results, especially in the mountainous northwestern region. Here, values of average R map
388 calculated by rain gauges were much higher than three type R_W , although they all have R
389 decreased from west to east. Noted that $ke-I$ empirical equation at Chilbolton station used in the
390 whole UK, will not always be accurate in regions with different rainfall characteristics. In terms
391 of R_W results, the three MPs obtained the same spatial pattern in rainfall erosivity, where R_{W-WDM6}
392 yielded the greatest geographical difference. It is clear that the proposed WRF-based estimated
393 method can capture more details of the spatial change of rainfall erosivity compares with the
394 traditional disdrometer-based method.

395 To evaluate the change in rainfall erosivity with time in the UK, the average value of all
396 the WRF grids covering the whole UK was calculated over 2013–2017 (Figure 10). The average
397 R_W trends of $R_{W-Morrison}$ and R_{W-TAA} were similar, both increasing from a minimum in 2013 to a
398 maximum in 2014, and then gradually decreasing from 2014 to 2017. The red line in Figure 10
399 indicates a series of mean values of the three MPs results, which varied from 36,782 to 51,600
400 $\text{MJ mm ha}^{-1} \text{h}^{-1} \text{y}^{-1}$ (mean: $43,216 \text{ MJ mm ha}^{-1} \text{h}^{-1} \text{y}^{-1}$).

401 The maximum values for $R_{W-Morrison}$ and R_{W-TAA} occurred in 2014, whereas that of R_{W-WDM6}
402 occurred in 2015. A sequence of extreme weather events occurred in the UK in 2014, including
403 major winter storms in late January to mid-February, which caused widespread flooding and
404 other economic losses, and greatly increased rainfall erosivity that year. However, the gauge-
405 based interpolation map shows the average annual rainfall amount for the years 2013–2017 were
406 884.9, 1014.0, 1008.5, 894.9, and 937.3 mm, respectively. The large rainfall erosivity difference
407 between 2014 and 2015, and the two years with similar rainfall amount, indicates that much
408 rainfall erosion occurs during the rainfall events of high intensity instead of simply high rainfall
409 amount. More notable variation pattern of rainfall erosivity may be found with longer simulation.
410 The strength of the proposed method lies on its ability to estimate large covering and long-term
411 rainfall erosivity.



412 **5 Conclusions**

413 This study presented a novel method for large-scale rainfall KE and erosivity estimation
414 based on high resolution WRF-derived DSDs. Three microphysical parameterizations schemes
415 (Morrison, WDM6, and Thompson aerosol-aware [TAA]) were designed to obtain raindrop size
416 distributions, rainfall KE and rainfall erosivity at the whole UK scale covering the period of
417 2013-2017. With validation by the long-term observations of a disdrometer, the WRF-based
418 rainfall erosivity showed acceptable performance at Chilbolton station. Among the three WRF
419 schemes, TAA performed best and was recommended for the future investigation. The results
420 revealed that high rainfall erosivity occurred in the west coast area in the UK. Compared with the
421 traditional empirical method, the proposed method can explain rainfall erosivity from a
422 microphysical perspective, and reflect more spatial variation due to changes in rainfall KE at the
423 whole-country scale. The development of a numerical weather prediction model therefore offers
424 an opportunity to better understand rainfall erosivity directly from its true definition. More
425 importantly, because the WRF model is able to be driven by the global reanalysis data to obtain
426 large-scale rainfall kinetic information, the proposed scheme can be easily applied to other
427 regions, especially in ungauged areas.

428 Although an acceptable rainfall erosivity estimation is obtained using the WRF model,
429 some uncertainties associated with it cannot be ignored. For example, as the MPs of WRF were
430 closely related to DSD, improper determination of MPs will introduce additional uncertainty.
431 The marked discrepancy among the three schemes (especially between Morrison and the others)
432 in this study underscored the possible uncertainty associated with R_w . Moreover, the
433 measurement error by disdrometer may also contaminate the evaluation process. For example,
434 when comparing the observed raindrop velocities based on the disdrometer at Bristol station with
435 their empirical values, we observed a dispersion of raindrops, with a number of drops showing
436 significant deviations. This velocity distribution resulted in an uncertainty in ke estimation.

437 In addition, other sources of uncertainty, such as temporal downscaling of rainfall and
438 point-to-area representative error by WRF, may introduce further uncertainty, which should be
439 put in perspective of future work. It is expected that more exploration of research areas with
440 different climatic and geographical characteristics would help us to establish a greater degree of
441 accuracy on this matter.



442 **Acknowledgments**

443 This work was supported by the National Natural Science Foundation of China (Nos.
444 41871299 and 41771424), and the National Key R & D Program of China (Nos.
445 2018YFB0505500, 2018YFB0505502). The authors acknowledge the British Atmospheric Data
446 Centre and the European Centre for Medium-range Weather Forecasts as the sources of data used
447 in the study.

448 The rain gauge datasets and Chilbolton disdrometers were sourced from the Met Office
449 Integrated Data Archive System (MIDAS). Both datasets are available from the NCAS British
450 Atmospheric Data Centre (<http://archive.ceda.ac.uk/>). The ERA-Interim data driving the WRF
451 model can be downloaded from the ECMWF Public Datasets web interface
452 (<https://www.ecmwf.int/>).

453 **References**

- 454 Alewell, C., Egli, M. and Meusburger, K. (2015). An attempt to estimate tolerable soil erosion
455 rates by matching soil formation with denudation in Alpine grasslands. *Journal of Soils and*
456 *Sediments* 15(6): 1383-1399.
- 457 Angulo-Martínez, M. and Barros, A. (2015). Measurement uncertainty in rainfall kinetic energy
458 and intensity relationships for soil erosion studies: An evaluation using PARSIVEL disdrometers
459 in the Southern Appalachian Mountains. *Geomorphology* 228: 28-40.
- 460 Angulo-Martínez, M., Beguería, S. and Kyselý, J. (2016). Use of disdrometer data to evaluate the
461 relationship of rainfall kinetic energy and intensity (KE-I). *Science of the Total Environment* 568:
462 83-94.
- 463 Angulo-Martínez, M., Beguería, S., Navas, A. and Machin, J. (2012). Splash erosion under
464 natural rainfall on three soil types in NE Spain. *Geomorphology* 175: 38-44.
- 465 Atlas, D., Srivastava, R. and Sekhon, R. S. (1973). Doppler radar characteristics of precipitation
466 at vertical incidence. *Reviews of Geophysics* 11(1): 1-35.
- 467 Atlas, D. and Ulbrich, C. W. (1977). Path-and area-integrated rainfall measurement by
468 microwave attenuation in the 1–3 cm band. *Journal of Applied Meteorology* 16(12): 1322-1331.



- 469 Beard, K. V. (1976). Terminal velocity and shape of cloud and precipitation drops aloft. *Journal*
470 *of the Atmospheric Sciences* 33(5): 851-864.
- 471 Bilotta, G., Grove, M. and Mudd, S. (2012). Assessing the significance of soil erosion.
472 *Transactions of the Institute of British Geographers* 37(3): 342-345.
- 473 Bonta, J. (2004). Development and utility of Huff curves for disaggregating precipitation
474 amounts. *Applied Engineering in Agriculture* 20(5): 641.
- 475 Borrelli, P., Robinson, D. A., Fleischer, L. R., Lugato, E., Ballabio, C., Alewell, C., Meusburger,
476 K., Modugno, S., Schütt, B. and Ferro, V. (2017). An assessment of the global impact of 21st
477 century land use change on soil erosion. *Nature Communications* 8(1): 1-13.
- 478 Brown, B. R., Bell, M. M. and Frambach, A. J. (2016). Validation of simulated hurricane drop
479 size distributions using polarimetric radar. *Geophysical Research Letters* 43(2): 910-917.
- 480 Brown, L. and Foster, G. (1987). Storm erosivity using idealized intensity distributions.
481 *Transactions of the ASAE* 30(2): 379-386.
- 482 Carter, C. E., Greer, J., Braud, H. and Floyd, J. (1974). Raindrop characteristics in south central
483 United States. *Transactions of the ASAE* 17(6): 1033-1037.
- 484 Cintineo, R., Otkin, J. A., Xue, M. and Kong, F. (2014). Evaluating the performance of planetary
485 boundary layer and cloud microphysical parameterization schemes in convection-permitting
486 ensemble forecasts using synthetic GOES-13 satellite observations. *Monthly Weather Review*
487 142(1): 163-182.
- 488 Ćurić, M., Janc, D., Vučković, V. and Kovačević, N. (2009). The impact of the choice of the
489 entire drop size distribution function on Cumulonimbus characteristics. *Meteorologische*
490 *Zeitschrift* 18(2): 207-222.
- 491 Dai, Q. and Han, D. (2014). Exploration of discrepancy between radar and gauge rainfall
492 estimates driven by wind fields. *Water Resources Research* 50(11): 8571-8588.
- 493 Dai, Q., Bray, M., Zhuo, L., Islam, T., and Han, D. (2017). A scheme for raingauge network
494 design based on remotely-sensed rainfall measurements. *Journal of Hydrometeorology* 18: 363-
495 379.



- 496 Dai, Q., Yang, Q., Han, D., Rico - Ramirez, M. A., and Zhang, S. (2019). Adjustment of radar -
497 gauge rainfall discrepancy due to raindrop drift and evaporation using the Weather Research and
498 Forecasting model and dual-polarization radar. *Water Resources Research* 55: 9211–9233.
- 499 Davison, P., Hutchins, M., Anthony, S., Betson, M., Johnson, C. and Lord, E. (2005). The
500 relationship between potentially erosive storm energy and daily rainfall quantity in England and
501 Wales. *Science of the Total Environment* 344(1-3): 15-25.
- 502 De Roo, A., Wesseling, C. and Ritsema, C. (1996). LISEM: a single - event physically based
503 hydrological and soil erosion model for drainage basins. I: theory, input and output. *Hydrological
504 Processes* 10(8): 1107-1117.
- 505 Dee, D. P., Uppala, S., Simmons, A., Berrisford, P., Poli, P., Kobayashi, S., Andrae, U.,
506 Balmaseda, M., Balsamo, G. and Bauer, d. P. (2011). The ERA - Interim reanalysis:
507 Configuration and performance of the data assimilation system. *Quarterly Journal of the Royal
508 Meteorological Society* 137(656): 553-597.
- 509 Defra (2009). Safeguarding our soils–A strategy for England. Defra, UK.
- 510 Doelling, I. G., Joss, J. and Riedl, J. (1998). Systematic variations of Z–R-relationships from
511 drop size distributions measured in northern Germany during seven years. *Atmospheric Research*
512 47: 635-649.
- 513 Duck, R. W. (1996). Regional variations of fluvial sediment yield in eastern Scotland. *Erosion
514 and Sediment Yield: Global and Regional Perspectives* 236:157-161.
- 515 Dudhia, J. (1989). Numerical study of convection observed during the winter monsoon
516 experiment using a mesoscale two-dimensional model. *Journal of the Atmospheric Sciences*
517 46(20): 3077-3107.
- 518 EA (2004). The state of soils in England and Wales. Environment Agency, UK.
- 519 Ek, M., Mitchell, K., Lin, Y., Rogers, E., Grunmann, P., Koren, V., Gayno, G. and Tarpley, J.
520 (2003). Implementation of Noah land surface model advances in the National Centers for
521 Environmental Prediction operational mesoscale Eta model. *Journal of Geophysical Research:*
522 *Atmospheres* 108(22):8851.



- 523 Evans, R. (1990). Soils at risk of accelerated erosion in England and Wales. *Soil use and*
524 *Management* 6(3): 125-131.
- 525 Fornis, R. L., Vermeulen, H. R. and Nieuwenhuis, J. D. (2005). Kinetic energy–rainfall intensity
526 relationship for Central Cebu, Philippines for soil erosion studies. *Journal of Hydrology* 300(1-4):
527 20-32.
- 528 Gilmore, M. S., Straka, J. M. and Rasmussen, E. N. (2004). Precipitation uncertainty due to
529 variations in precipitation particle parameters within a simple microphysics scheme. *Monthly*
530 *Weather Review* 132(11): 2610-2627.
- 531 Hanel, M., Máca, P., Bašta, P., Vlnas, R. and Pech, P. (2016). The rainfall erosivity factor in the
532 Czech Republic and its uncertainty. *Hydrology and Earth System Sciences* 20(10): 4307-4322.
- 533 Hong, S.-Y., Lim, K.-S. S., Lee, Y.-H., Ha, J.-C., Kim, H.-W., Ham, S.-J. and Dudhia, J. (2010).
534 Evaluation of the WRF double-moment 6-class microphysics scheme for precipitating
535 convection. *Advances in Meteorology* 2010.
- 536 Hudson, N. (1963). Raindrop size distribution in high intensity storms. *Rhodesian Journal of*
537 *Agricultural Research* 1(1): 6-11.
- 538 Islam, T., Rico-Ramirez, M. A., Thurai, M. and Han, D. (2012). Characteristics of raindrop
539 spectra as normalized gamma distribution from a Joss–Waldvogel disdrometer. *Atmospheric*
540 *Research* 108: 57-73.
- 541 Janjić, Z. I. (1994). The step-mountain eta coordinate model: Further developments of the
542 convection, viscous sublayer, and turbulence closure schemes. *Monthly Weather Review* 122(5):
543 927-945.
- 544 Johnson, M., Jung, Y., Dawson, D. T. and Xue, M. (2016). Comparison of simulated
545 polarimetric signatures in idealized supercell storms using two-moment bulk microphysics
546 schemes in WRF. *Monthly Weather Review* 144(3): 971-996.
- 547 Jones, D. M. A. (1959). The shape of raindrops. *Journal of the Atmospheric Sciences* 16(1): 511-
548 515.



- 549 Jung, Y., Xue, M. and Zhang, G. (2010). Simulations of polarimetric radar signatures of a
550 supercell storm using a two-moment bulk microphysics scheme. *Journal of Applied Meteorology*
551 and *Climatology* 49(1): 146-163.
- 552 Kain, J. S. (2004). The Kain–Fritsch convective parameterization: an update. *Journal of Applied*
553 *Meteorology* 43(1): 170-181.
- 554 Kinnell, P. (1981). Rainfall intensity-kinetic energy relationships for soil loss prediction. *Soil*
555 *Science Society of America Journal* 45(1): 153-155.
- 556 Kinnell, P. and Risse, L. (1998). USLE-M: empirical modeling rainfall erosion through runoff
557 and sediment concentration. *Soil Science Society of America Journal* 62(6): 1667-1672.
- 558 Lim, K.-S. S. and Hong, S.-Y. (2010). Development of an effective double-moment cloud
559 microphysics scheme with prognostic cloud condensation nuclei (CCN) for weather and climate
560 models. *Monthly Weather Review* 138(5): 1587-1612.
- 561 Lim, Y. S., Kim, J. K., Kim, J. W., Park, B. I. and Kim, M. S. (2015). Analysis of the
562 relationship between the kinetic energy and intensity of rainfall in Daejeon, Korea. *Quaternary*
563 *International* 384: 107-117.
- 564 Marshall, J. S. and Palmer, W. M. K. (1948). The distribution of raindrops with size. *Journal of*
565 *Meteorology* 5(4): 165-166.
- 566 McIsaac, G. (1990). Apparent geographic and atmospheric influences on raindrop sizes and
567 rainfall kinetic energy. *Journal of Soil and Water Conservation* 45(6): 663-666.
- 568 Meshesha, D. T., Tsunekawa, A. and Haregeweyn, N. (2019). Influence of raindrop size on
569 rainfall intensity, kinetic energy, and erosivity in a sub-humid tropical area: a case study in the
570 northern highlands of Ethiopia. *Theoretical and Applied Climatology* 136(3-4): 1221-1231.
- 571 Meshesha, D. T., Tsunekawa, A., Tsubo, M., Haregeweyn, N. and Adgo, E. (2014). Drop size
572 distribution and kinetic energy load of rainfall events in the highlands of the Central Rift Valley,
573 Ethiopia. *Hydrological Sciences Journal* 59(12): 2203-2215.
- 574 Meshesha, D. T., Tsunekawa, A., Tsubo, M., Haregeweyn, N. and Tegegne, F. (2016).
575 Evaluation of kinetic energy and erosivity potential of simulated rainfall using Laser
576 Precipitation Monitor. *Catena* 137: 237-243.



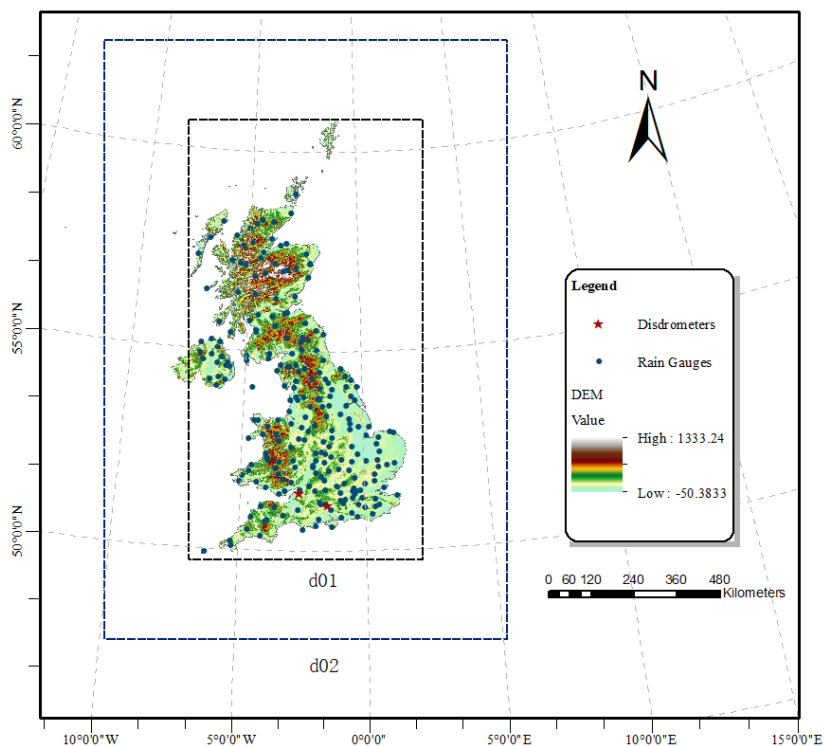
- 577 Mikoš, M., Jošt, D. and Petkovšek, G. (2006). Rainfall and runoff erosivity in the alpine climate
578 of north Slovenia: a comparison of different estimation methods. *Hydrological sciences journal*
579 51(1): 115-126.
- 580 Mlawer, E. J., Taubman, S. J., Brown, P. D., Iacono, M. J. and Clough, S. A. (1997). Radiative
581 transfer for inhomogeneous atmospheres: RRTM, a validated correlated - k model for the
582 longwave. *Journal of Geophysical Research: Atmospheres* 102(14): 16663-16682.
- 583 MO (2012). Met Office Integrated Data Archive System (MIDAS) land and marine surface
584 stations data (1853 - current).
- 585 Montopoli, M., Marzano, F. S. and Vulpiani, G. (2008). Analysis and synthesis of raindrop size
586 distribution time series from disdrometer data. *IEEE Transactions on Geoscience and Remote*
587 *Sensing* 46(2): 466-478.
- 588 Morgan, R. (1985). Assessment of soil erosion risk in England and Wales. *Soil use and*
589 *Management* 1(4): 127-131.
- 590 Morrison, H., Milbrandt, J. A., Bryan, G. H., Ikeda, K., Tessorndorf, S. A. and Thompson, G.
591 (2015). Parameterization of cloud microphysics based on the prediction of bulk ice particle
592 properties. Part II: Case study comparisons with observations and other schemes. *Journal of the*
593 *Atmospheric Sciences* 72(1): 312-339.
- 594 Morrison, H., Thompson, G. and Tatarskii, V. (2009). Impact of cloud microphysics on the
595 development of trailing stratiform precipitation in a simulated squall line: Comparison of one-
596 and two-moment schemes. *Monthly weather review* 137(3): 991-1007.
- 597 Nyssen, J., Vandenreyken, H., Poesen, J., Moeyersons, J., Deckers, J., Haile, M., Salles, C. and
598 Govers, G. (2005). Rainfall erosivity and variability in the Northern Ethiopian Highlands.
599 *Journal of Hydrology* 311(1-4): 172-187.
- 600 O'Neill, D. (2007). The total external environmental costs and benefits of agriculture in the UK.
601 Environment Agency, UK.



- 602 Panagos, P., Ballabio, C., Borrelli, P., Meusburger, K., Klik, A., Rousseva, S., Tadić, M. P.,
603 Michaelides, S., Hrabal *kov* á M. and Olsen, P. (2015a). Rainfall erosivity in Europe. *Science of*
604 *the Total Environment* 511: 801-814.
- 605 Panagos, P., Borrelli, P., Poesen, J., Ballabio, C., Lugato, E., Meusburger, K., Montanarella, L.
606 and Alewell, C. (2015b). The new assessment of soil loss by water erosion in Europe.
607 *Environmental Science & Policy* 54: 438-447.
- 608 Park, S., Mitchell, J. and Bubenzer, G. (1982). Splash erosion modeling: physical analysis.
609 *Transactions of the ASAE* 25:357-361.
- 610 Petan, S., Rusjan, S., Vidmar, A. and Mikoš, M. (2010). The rainfall kinetic energy–intensity
611 relationship for rainfall erosivity estimation in the mediterranean part of Slovenia. *Journal of*
612 *Hydrology* 391(3-4): 314-321.
- 613 Prigent, C. (2010). Precipitation retrieval from space: An overview. *Comptes Rendus Geoscience*
614 342(4-5): 380-389.
- 615 Renard, K. G., Foster, G. R., Weesies, G., McCool, D. and Yoder, D. (1997). Predicting soil
616 erosion by water: a guide to conservation planning with the Revised Universal Soil Loss
617 Equation (RUSLE), United States Department of Agriculture Washington, DC.
- 618 Rosewell, C. J. (1986). Rainfall kinetic energy in eastern Australia. *Journal of Climate and*
619 *Applied Meteorology* 25(11): 1695-1701.
- 620 Sanchez-Moreno, J. F., Mannaerts, C. M., Jetten, V. and Löffler-Mang, M. (2012). Rainfall
621 kinetic energy–intensity and rainfall momentum–intensity relationships for Cape Verde. *Journal*
622 *of Hydrology* 454: 131-140.
- 623 Sempere - Torres, D., Porrà, J. M. and Creutin, J. D. (1998). Experimental evidence of a general
624 description for raindrop size distribution properties. *Journal of Geophysical Research:*
625 *Atmospheres* 103(2): 1785-1797.
- 626 Song, Y., Han, D. and Rico-Ramirez, M. A. (2017). High temporal resolution rainfall rate
627 estimation from rain gauge measurements. *Journal of Hydroinformatics* 19(6): 930-941.
- 628 Thompson, G. and Eidhammer, T. (2014). A study of aerosol impacts on clouds and precipitation
629 development in a large winter cyclone. *Journal of the Atmospheric Sciences* 71(10): 3636-3658.



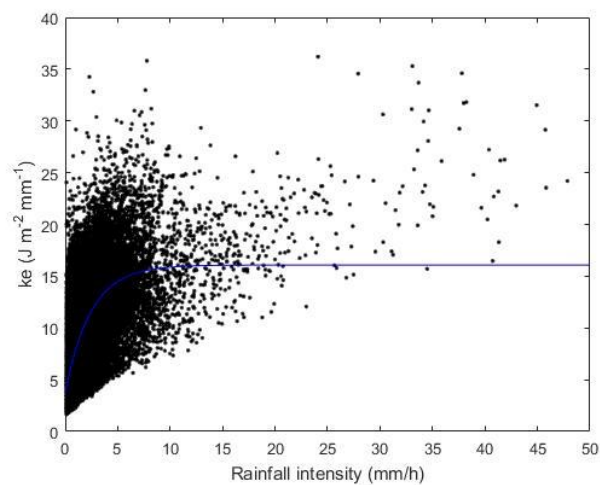
- 630 Uplinger, W. (1981). A new formula for raindrop terminal velocity. Conference on Radar
631 Meteorology, 20 th, Boston, MA.
- 632 Van Dijk, A., Bruijnzeel, L. and Rosewell, C. (2002). Rainfall intensity–kinetic energy
633 relationships: a critical literature appraisal. *Journal of Hydrology* 261(1-4): 1-23.
- 634 Wang, L., Shi, Z., Wang, J., Fang, N., Wu, G. and Zhang, H. (2014). Rainfall kinetic energy
635 controlling erosion processes and sediment sorting on steep hillslopes: a case study of clay loam
636 soil from the Loess Plateau, China. *Journal of Hydrology* 512: 168-176.
- 637 Weiss, L. L. (1964). Ratio of true to fixed-interval maximum rainfall. *Journal of the Hydraulics*
638 *Division* 90(1): 77-82.
- 639 Williams, R. and Sheridan, J. (1991). Effect of rainfall measurement time and depth resolution
640 on EI calculation. *Transactions of the ASAE* 34(2): 402-0406.
- 641 Wischmeier, W. H. and Smith, D. D. (1958). Rainfall energy and its relationship to soil loss. *Eos,*
642 *Transactions American Geophysical Union* 39(2): 285-291.
- 643 Wischmeier, W. H. and Smith, D. D. (1978). Predicting rainfall erosion losses-a guide to
644 conservation planning. Department of Agriculture, Science and Education Administration, US.
- 645 Xie, Y., Yin, S., Liu, B., Nearing, M. A. and Zhao, Y. (2016). Models for estimating daily
646 rainfall erosivity in China. *Journal of Hydrology* 535: 547-558.
- 647 Yang, Q., Dai, Q., Han, D., Chen, Y., and Zhang, S. (2019). Sensitivity analysis of raindrop size
648 distribution parameterizations in weather research and forecasting rainfall simulation.
649 *Atmospheric Research* 228:1-13.
- 650
- 651



652

653 **Figure 1.** Location of rain gauges, Joss–Waldvogel disdrometer (JWD) at Chilbolton
654 Observatory, OTT Parsivel² disdrometer (OPD) at Bristol Observatory and configurations of
655 domain setups in the WRF model.

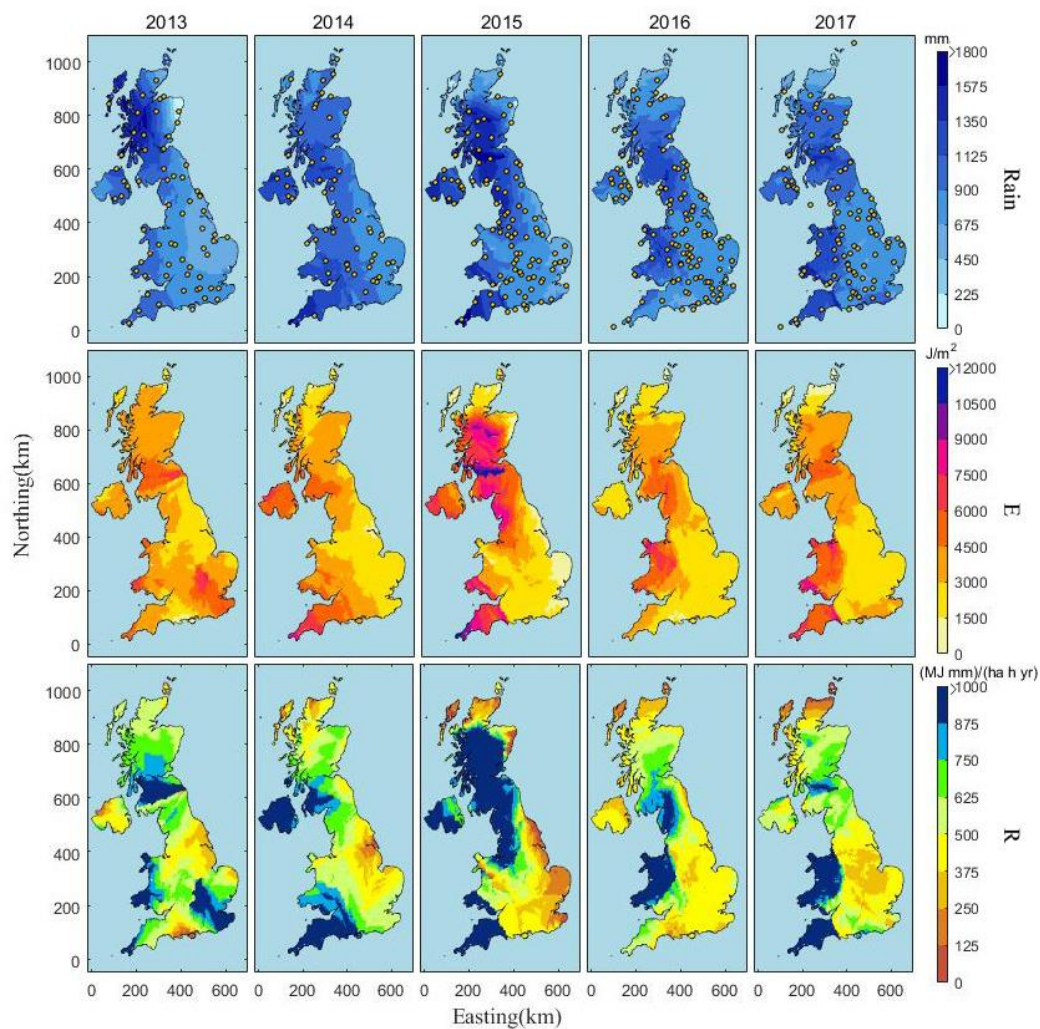
656



657

658 **Figure 2.** The fitted relationship of $ke-I$ based on exponential regression (2004–2013).

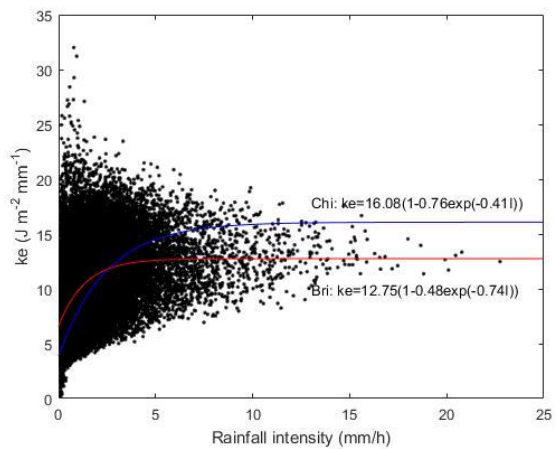
659



660

661 **Figure 3.** Gauge-based interpolation maps of annual rainfall amount (*Rain*), rainfall kinetic
662 energy (*E*) and rainfall erosivity (*R*) in 2013-2017.

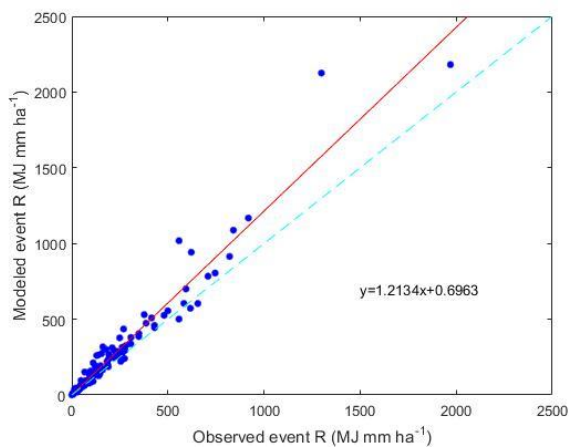
663



664

665 **Figure 4.** Relationship of $ke-I$ at Bristol station.

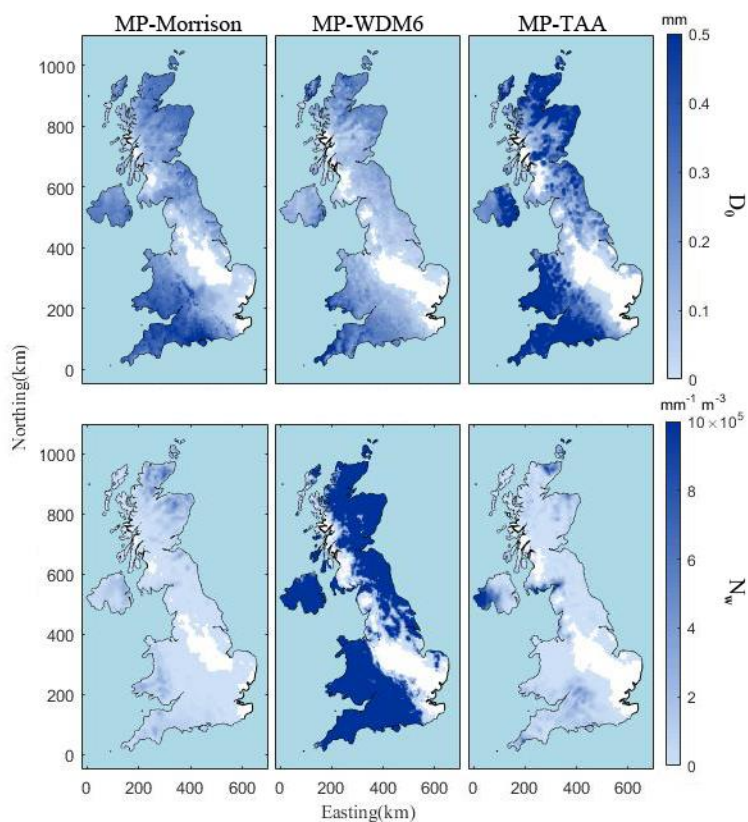
666



667

668 **Figure 5.** Comparison of observed and modeled event rainfall erosivity covering the period of
669 2016–2019.

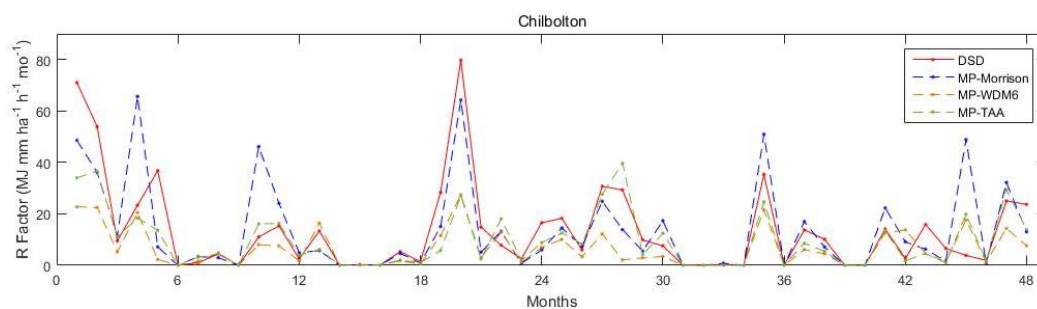
670



671

672 **Figure 6.** Map of average WRF DSD D_0 and N_w (January 10, 2013).

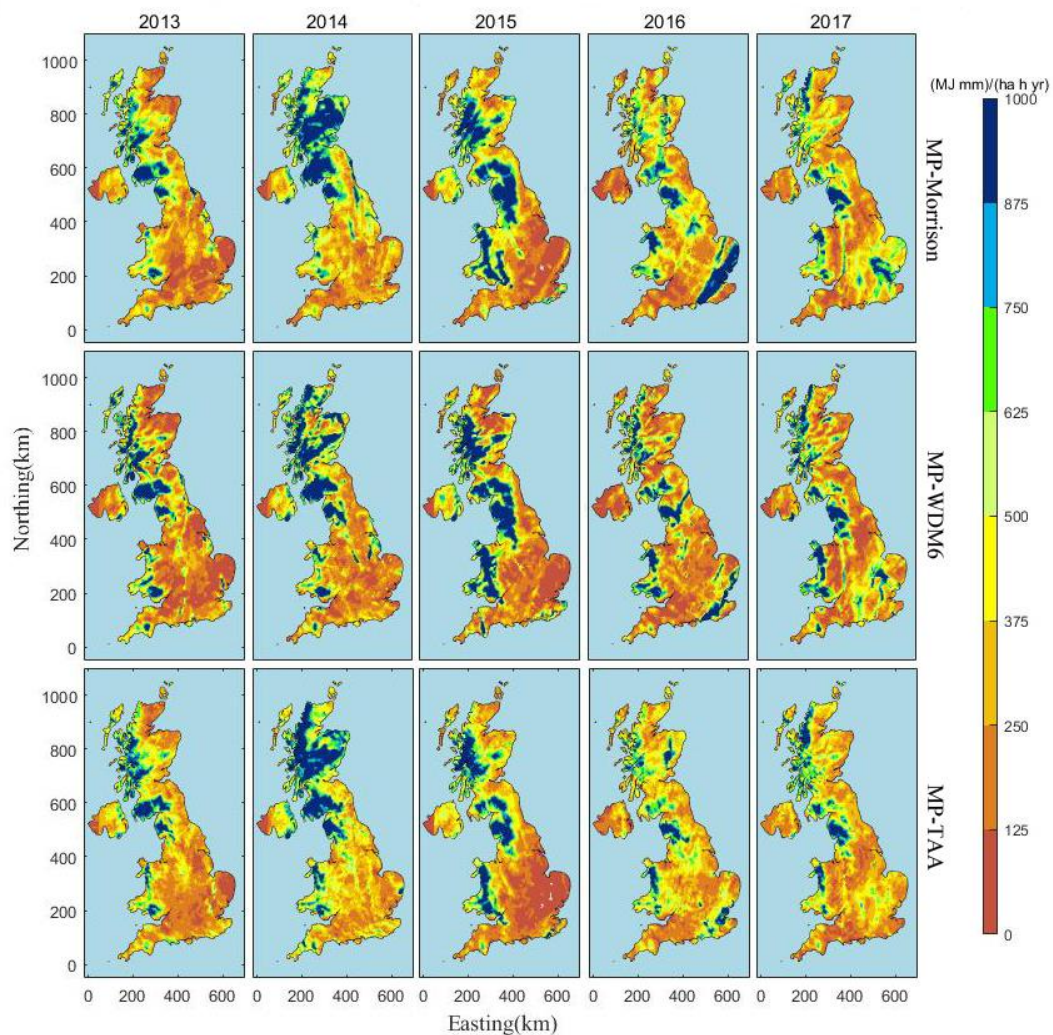
673



674

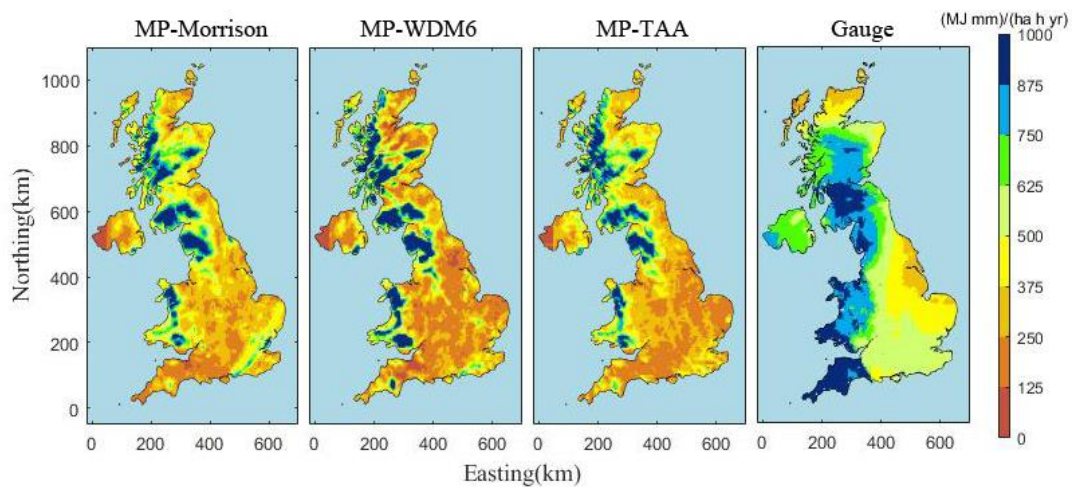
675 **Figure 7.** Comparison of disdrometer- and WRF-derived monthly rainfall erosivity estimations
676 at Chilbolton station.

677



678
679 **Figure 8.** R_W maps of the whole UK for different years.

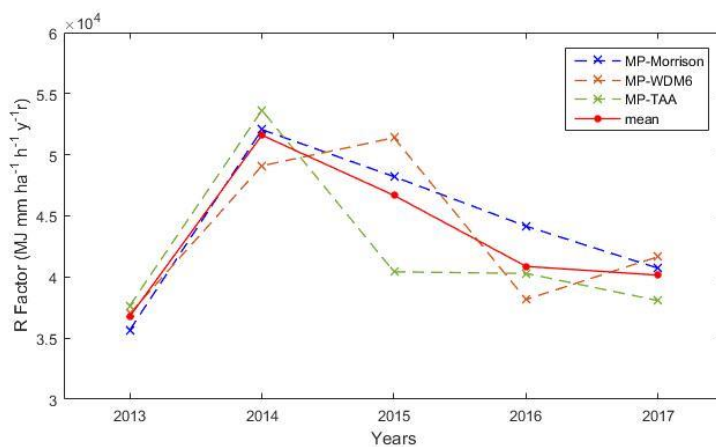
680



681

682 **Figure 9.** The 5-year (2013–2017) average R maps based on WRF grids and rain gauge
683 interpolation.

684



685

686 **Figure 10.** The average R_W of all the WRF grids covering the whole UK (2013–2017).

687



688 **Table 1.** Relationship of $ke-I$ at Chilbolton Station.

ID	Equation	Calibration R^2	Validation R^2
I	$ke = 16.08(1 - 0.76e^{-0.41I})$	0.50	0.45
II	$ke = 8.65 + 6.39 \lg(I)$	0.48	0.43
III	$ke = 10.19 - 1.05/I$	0.29	0.25
IV	$ke = 8.65 + 2.78 \ln(I)$	0.48	0.43
V	$ke = 8.12I^{0.34}$	0.50	0.45

689

690



691 **Table 2.** The configurations of WRF model for two nested domains.

Domain	Domain size (km)	Grid Spacing (km)	Grid size	Downscaling ratio
d01	1,125 × 1,675	25	45 × 67	-
d02	655 × 1,230	5	131 × 246	1:5

692

693



694 **Table 3.** Indicators comparison between R_D and three type R_W at Chilbolton station on monthly
695 scale.

Indicators	MP-Morrison	MP-WDM6	MP-TAA
Pearson	0.71	0.77	0.79
MAE	8.05	8.42	6.51
R^2	0.42	0.31	0.54

696